

# Force-Based Viscosity and Elasticity Measurements for Material Biomechanical Characterisation with a Collaborative Robotic Arm

Luca Beber<sup>1,2</sup>, Edoardo Lamon<sup>1</sup>, Giacomo Moretti<sup>3</sup>, Matteo Saveriano<sup>3</sup>,  
Luca Fambri<sup>3</sup>, Luigi Palopoli<sup>1</sup>, and Daniele Fontanelli<sup>3</sup>

**Abstract**—Diagnostic activities, such as ultrasound scans and palpation, are relatively low-cost. They play a crucial role in the early detection of health problems and in assessing their progression. However, they are also error-prone activities, which require highly skilled medical staff. The use of robotic solutions can be key to decreasing the inherent subjectivity of the results and reducing the waiting list. For a robot to perform palpation or ultrasound scans, it must effectively manage physical interactions with the human body, which greatly benefits from precise estimation of the patient’s tissue biomechanical properties. This paper assesses the accuracy and precision of a robotic system in estimating the viscoelastic parameters of various materials, including some tests on ex vivo tissues as a preliminary proof-of-concept demonstration of the method’s applicability to biological samples. The measurements are compared against a ground truth derived from silicone specimens with different viscoelastic properties, characterised using a high-precision instrument. Experimental results show that the robotic system’s accuracy closely matches the ground truth, increasing confidence in the potential use of robots for such clinical applications.

**Index Terms**—Viscoelastic Estimation, Dimensionality Reduction, Biomechanical Characterisation.

## I. INTRODUCTION

UNDERSTANDING the mechanical properties of biological materials is crucial for a wide range of medical applications. For example, in prosthetics and tissue engineering, synthetic implants or repairs must replicate the specific characteristics of native tissues. In robotics, any medical procedure involving direct interaction between a robot and the human body can benefit from knowledge of the tissue’s mechanical properties in the operative field. This information can improve the control accuracy during a surgical cut, help produce high-quality haptic feedback for teleoperated procedures [1], and enable a fine grained localisation of the tool on or inside the body (e.g., to identify the intercostal regions on the rib cage [2]). In robot-based diagnosis, tissue characteristics can be used as indicators of various diseases. For example, a localized region with increased elasticity in the abdominal area may indicate the presence of a neoplastic lesion. This observation is supported by the findings of [3] on selected tissues. Similar examinations can be used to assess tissue ageing [4] or to detect systemic sclerosis (SSC) [5].

Among the mechanical properties of human tissues, elasticity and viscosity are of particular significance. Elasticity refers to the material’s ability to deform under stress and subsequently return to its original shape once the stress is removed. Viscosity measures the material’s resistance to flow or deformation under continuous stress. Different tissues and organs exhibit a unique viscoelastic behaviour due to the combination of elastic and viscous responses; therefore, accurately characterising these parameters is crucial for accurate diagnosis.

Robotic systems offer clear advantages for analyzing mechanical properties. Unlike other mechanical devices, a robot can utilize its kinematics to explore large areas of the body (just as a human physician would do). For example palpations for medical purposes are often performed in anatomically challenging areas, such as the armpit for lymph node examinations, where standard testing devices are impractical. A robotic arm provides the necessary degrees of freedom to navigate these complex regions, ensuring consistent and repeatable assessments, and, thanks to the flexibility of the device, can also be used for other medical practices, making it also economically convenient for specialised instrumentation capable only of performing elasticity measurements. Implementing precise viscoelastic contact models allows robots to determine the contact area, interaction forces, and penetration depth of the end-effector into the tissue or body [2]. However, applying robotic diagnosis in real-time presents challenges: inaccurate estimation of viscoelastic parameters can lead to significant diagnostic errors, patient discomfort, and, in the worst case, injury. This leads to the central research question addressed in this paper: how accurately can a robotic system equipped with standard force sensors estimate the viscoelastic parameters of human tissue?

*Viscoelastic properties estimation:* Several techniques have been developed for the characterisation of the viscoelastic properties of human tissue. For instance, magnetic resonance imaging (MRI) is used to assess the viscoelastic properties of biological tissues by measuring shear wave velocity [6]–[8]. Magnetic resonance elastography (MRE) is a powerful, non-invasive technique but is constrained by expensive and complex instrumentation that requires specialised personnel, making it unsuitable for large-scale initial screening applications. In contrast, ultrasound elastography estimate the viscoelastic properties of a material by analysing the propagation of ultrasound waves [9]–[13]. Ultrasound elastography

<sup>1</sup>Department of Information Engineering and Computer Science, Università di Trento, Trento, Italy. luca.beber@unitn.it

<sup>2</sup>DRIM, Ph.D. of national interest in Robotics and Intelligent Machines.

<sup>3</sup>Department of Industrial Engineering, Università di Trento, Trento, Italy.

is promising but suffers from operator dependence and is primarily useful for comparative rather than absolute stiffness measurements. Moreover, it requires expensive ultrasound equipment. Cretu et al. [14] proposed a method to estimate the elastic modulus by measuring the deformation of the soft body with a laser and then using a neural network-based estimator. Traditional dynamic testing methods, such as rheometry and dynamic mechanical analysis (DMA), provide high-precision viscoelastic measurements by applying oscillatory forces at controlled frequencies. However, these techniques require specialised laboratory equipment and are limited to small, isolated samples, making them impractical for in situ or large-scale applications. In contrast, the proposed robotic approach enables real-time viscoelasticity estimation over larger surface areas while reducing operator dependency, bridging the gap between high-precision laboratory techniques and deployable clinical solutions. Furthermore, as demonstrated in our prior work [2], this approach is also suitable for robotic telehealth applications, where knowledge of the mechanical properties of contacted tissue can substantially enhance operational safety.

*Force response models:* Viscoelastic parameters estimation of a material by means of contact forces relies on appropriate models for the force response. The literature offers simple linear models such as the Kelvin-Voigt or the Maxwell models [15]. These models allow for a fast parameter estimation, but are also known for their limited accuracy, especially in the case of contacts with small penetration [16]. The Hunt-Crossley model is a potentially better alternative [16]–[18] for its ability to encode the nonlinear behaviour of the forces resulting from the three-dimensional nature of the contact. The downside is that the model requires a complex procedure to identify the model parameters. The fact that these parameters do not have direct physical meaning adds much to the complexity of the problem (viscosity and elasticity cannot be expressed as a direct function of the *stiffness* and *damping* of the model). To simplify the parameter estimation, these models are often applied in conjunction with different estimation techniques, including nonlinear least squares regression [19], [20] and Kalman filtering [16], [17], [21], [22]. This is done assuming a known penetration depth [17], a condition that is impractical in real-world exams like palpation.

*Paper contribution:* This paper presents a method for estimating the local and global viscoelastic properties of soft materials using a robotic system. The approach enables accurate reconstruction of contact forces and can be applied both offline and online. Estimating viscoelastic parameters using non-rigid contact models while accounting for measurement uncertainties requires a physical system capable of applying controlled perturbations to the soft body. As shown in Fig. 1, our choice fell on a robotic arm equipped with an indenter (as end effector) and with a precise 6-axis force/torque sensor, that is mounted between the robot flange and the indenter. Since it is known in the literature that under static or quasi-static conditions it is possible to estimate only the elasticity value [23]–[26], viscosity and penetration are usually assumed known, because their estimate requires a much more complex analysis under dynamic conditions. To overcome this limitation, we exploited the *Dimensionality Reduction (DR)* [27]

method, commonly employed in tribology. This method allows us to reduce to a 1D dynamic equation the 3D contact between an axial-symmetric indenter and a soft, flat surface. The equation establishes a relation between the elasticity and viscosity modulus, and the penetration inside the material. Since the method exploits the geometry of the elements in contact, it can be applied to generic indenter shapes, which are, in our case, the robot end effector tips. This allows us to lift an important restriction of previous approaches: the use of spherical indenter tips [28] imposed by the Hertzian theory. The paper presents the main ideas underlying the described process and the results of the characterisation of the measurement system using different classes of materials with known model parameters.

A subset of the mentioned contributions have been presented in a conference paper [29], where an elastic characterisation of testing foams has been proposed to validate the robot arm as an instrument. In this paper, we extend the method and the results of [29] in several respects: 1) we include the viscosity in the DR, 2) we propose an online procedure to perform not only local point-wise measurements but also continuous measurements on wider surfaces, which present different local characteristics, 3) we repeat the evaluation of the indenter tip with silicones and extend it to quartic indenters, which were not considered in our previous conference paper. An important practical and theoretical implication of these improvements is in the paper experimental section, where we analyse both silicones with homogeneous viscoelasticity and silicones containing harder material inside, which mimics the presence of stiffer tissues embodied in softer parts. In [30] we exploited the online point-wise algorithm to estimate the penetration inside the soft tissue and the parameters to reconstruct the contact force, enabling the detection of foreign masses in soft materials. In this work, we use those results to compare the online estimation of elasticity with a static estimation and expand the algorithm to have a continuous estimation of the viscoelasticity parameters. Finally, a preliminary proof-of-concept experiment was conducted to validate the proposed method's ability to estimate the viscoelastic properties of an ex vivo tissue. Measurements were performed both on healthy tissue and on tissue containing a stiffer intrusion.

The findings in this manuscript, which confirm and extend the ones on foams of the previous work, show that the level of accuracy in viscoelasticity estimation and in force reconstruction reached by the solution is promising for biomedical applications in the near future.

## II. CONTACT MODEL WITH THE DIMENSIONALITY REDUCTION MODEL

This section presents the fundamental concepts behind the dimensionality reduction method (DR), proposed by Popov et al. [27] and describing the contact behaviour between an axial symmetric indenter and a soft material. The formulation for the elastic contributions was presented in our previous work [29], while in this study we include the viscosity component in the contact model. The following section shows how is possible to approximate the response of soft material modelling it as a series of spring-damper elements.

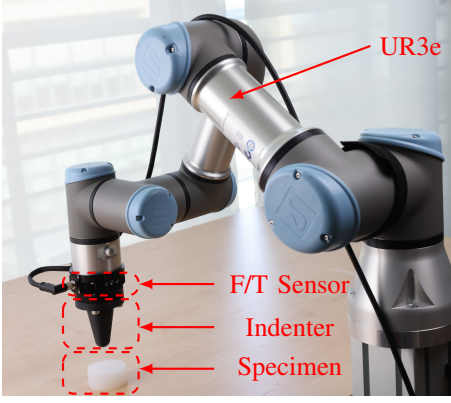


Fig. 1. Experimental setup consisting of a 6-DoF Ur3e robotic arm, a 6-axis F/T sensor, a 3D printed indenter, and the specimen that is being tested.

### A. Elastic Force Model

The main idea of the DR method is that the 3D contact between an indenter of an axially symmetric arbitrary shape and the surface of an elastic object can be modelled by resorting to a one-dimensional equivalent model, in which the elastic body is described through a one-dimensional linearly elastic foundation, consisting of a set of identical springs positioned at a small distance from each other [27]. The resulting contact stiffness of each spring is a function of the elastic modulus of the material and of the distance between neighbour springs, i.e.,

$$\Delta k_z = E^* \Delta x, \quad (1)$$

with  $\Delta k_z$  being the stiffness of a single spring,  $\Delta x$  the spacing between the springs and  $E^*$  the so-called effective elastic modulus.

An effective elastic modulus  $E^*$  for the substrate can be extracted knowing the Poisson ratio  $\nu$  and the material elastic modulus  $E_f$ :

$$E^* = \frac{E_f}{1 - \nu^2}, \quad (2)$$

which stems from the assumption that the material is in plane-stress in one of the directions perpendicular to the indentation direction, and in plane-strain in the the third direction. The force exerted by each spring is expressed as a function of the deformation using (1) and (2), that is

$$\Delta f_{N,i} = \Delta k_z u_{z,i} = \frac{E_f}{1 - \nu^2} \Delta x u_{z,i}, \quad (3)$$

where  $u_{z,i}$  is the local displacement of the  $i$ -th spring. The penetration depth of the indenter is a function of its shape and of the position of the tip of the end-effector. For example, for a flat indenter, the spring deformation will be equal throughout the entire contact area, whereas with a spherical indenter the spring in the centre of the tip will be more compressed than the springs on the sides.

**Spherical indenter.** For a spherical indenter with radius  $R$ , the three dimensional contact problem can be reformulated as an equivalent one-dimensional problem, in which a linear elastic foundation is indented by a circular indenter with radius  $R_1 = R/2$  (see Fig. 2 for reference). Using the

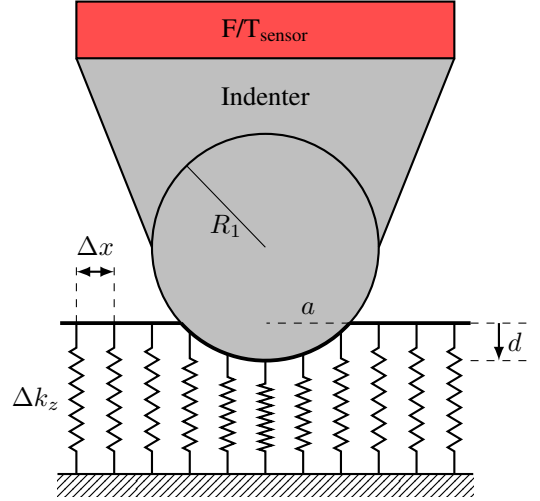


Fig. 2. Spherical indenter inside the elastic foundation.  $d$  is the penetration,  $a$  is the projection of the surface of the circle in contact, and  $R_1$  is the equivalent radius of the 3D sphere.

Hertzian theory, the circular profile of the indenter sphere can be further approximated with a 2D parabolic interpolating profile  $g(x) = \frac{x^2}{2R_1}$  [28]. More precisely, let  $d$  be the depth of penetration into the material. The force exerted by an individual spring will vary according to its position along the profile of the indenter. In the limit case of an infinitesimal space between the springs, i.e.,  $\Delta x \simeq dx$ , the infinitesimal force contribution of a single spring element (as given by equation (3)) can be rewritten as:

$$df_N = \frac{E_f}{1 - \nu^2} \left( d - \frac{x^2}{2R_1} \right) dx. \quad (4)$$

The portion of the indenter in contact with the surface is  $a = \sqrt{2R_1 d}$ , hence to obtain the total normal force generated by the material, (4) is integrated from  $-a$  to  $a$ , obtaining

$$\begin{aligned} F_N(d) &= \int_{-a}^a df_N = \int_{-a}^a \left[ \frac{E_f}{1 - \nu^2} \left( d - \frac{x^2}{2R_1} \right) \right] dx = \\ &= \int_{-\sqrt{2R_1 d}}^{\sqrt{2R_1 d}} \left[ \frac{E_f}{1 - \nu^2} \left( d - \frac{x^2}{2R_1} \right) \right] dx = \\ &= \frac{4}{3} \frac{E_f}{1 - \nu^2} d \sqrt{2R_1 d}. \end{aligned} \quad (5)$$

Substituting again  $R_1 = R/2$ , the result obtained in (5) is the same as in the Hertzian theory.

**Generalisation to symmetric indenters.** The previous formulation can be extended to any axially symmetric indenter. Indeed, by defining the plane indenter geometry, the contact problem is modelled as a 2D problem in combination with the linear elastic foundation described above. The reduced planar profile for a generic axial symmetric shape can be expressed as

$$g_n(x) = \tilde{c}_n |x|^n, \quad (6)$$

where  $n$  is a generic positive number, and  $\tilde{c}_n = k_n c_n$  is a constant, given by the product of a shape factor  $c_n$  defining the shape of the 3D profile ( $z = c_n r^n$ , where  $(r, z)$  are polar coordinates), and  $k_n$  is a constant computed following the rule

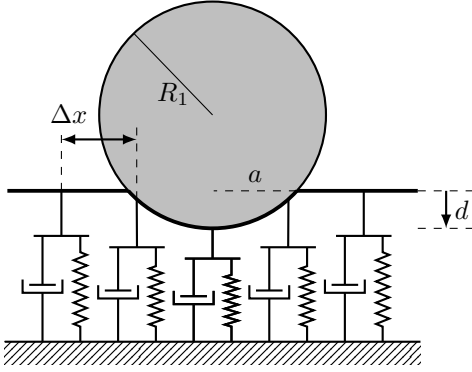


Fig. 3. Schematic of the updated model containing the damper that describes the viscous behaviour of the material.

given by Hess [27]. Finally, the normal force can be written as

$$F_N(d) = \frac{2n}{n+1} \frac{E_f}{1-\nu^2} \bar{c}_n^{-\frac{1}{n}} d^{\frac{n+1}{n}}. \quad (7)$$

It is possible to obtain the force equation for the flat indenter and an indenter described by a function of degree four ( $n = 4$ ) as

$$F_{N,\text{flat}}(d) = \frac{E_f}{1-\nu^2} 2ad, \quad (8)$$

$$F_{N,n=4}(d) = \frac{8}{5} \frac{E_f}{1-\nu^2} (2.667c_4)^{-\frac{1}{n}} d^{\frac{5}{4}}. \quad (9)$$

### B. Viscous Force Model

The dimensionality reduction method can be extended to describe the viscoelastic behaviour of the flexible substrate. Let us take the same reduced system as in Fig. 2 where the springs are substituted by dampers. Popov et al. [27] have shown that the expression of the force contribution of a single damper has the following form

$$\Delta f_{D,i} = \frac{2}{1-\nu} \eta \Delta x \dot{u}_{z,i}, \quad (10)$$

where  $\dot{u}_{z,i}$  is the penetration rate. Noting that, for a generic indenter,  $u_{z,i} = d - g_n(x)$ , we can assume  $\dot{u}_{z,i} = \dot{d}$ . Hence, the force generated by a single spring-damper (Kelvin-Voigt) element (assumed infinitesimal, i.e.,  $\Delta x \simeq dx$ ) is the sum of (10) and (3), giving

$$df_{DR,i} = \frac{E_f}{1-\nu^2} (d - g_n(x)) dx + \frac{2}{1-\nu} \eta \dot{d} dx. \quad (11)$$

Fig. 3 shows the schematic of a spherical indenter in contact with a material modelled by multiple parallel Kelvin-Voigt elements. Similarly to (5), the force (11) can be integrated along the incontact surface of a spherical indenter to get the total force as a function of the penetration into the material, i.e.,

$$F_{DR}(d) = \frac{4}{3} \frac{E_f}{1-\nu^2} \sqrt{R} d d + \frac{4}{1-\nu} \eta \sqrt{R} d \dot{d}. \quad (12)$$

A similar result could be obtained considering an indenter with generic shape, leading, of course, to a more complicated expression.

### C. Background on Offline Elasticity Estimation

As discussed in [29], if the contact force in static conditions (i.e., at slow deformation rates that render viscous forces negligible) is measured by a sensor mounted in series to the indenter, a least square algorithm can be used to estimate the value of the elasticity modulus that minimises

$$\mathcal{L} = \sum_{j=i}^L (F_{\text{sensor},j} - F_N(d_j))^2, \quad (13)$$

where  $L$  is the number of acquired measurement points,  $F_{\text{sensor},j}$  is the  $j$ -th force sample and  $d_j$  is the  $j$ -th penetration value. A challenge for the estimation problem is related to the difficulties to locate the precise position of the specimen surface within the robot frame, since the detection of the contact force is affected by uncertainties. Therefore, the least square problem is cast by retaining the surface position as one of the unknowns and including a constraint on the value of the force:

$$\begin{aligned} \underset{E_f, z_{\text{surf}}}{\text{argmin}} \quad & \mathcal{L} \\ \text{s.t.} \quad & -F_{\text{unc}} \leq F(z_{\text{surf}}) \leq F_{\text{unc}}. \end{aligned} \quad (14)$$

where  $z_{\text{surf}}$  and  $z_{\text{EE}}$  are the  $z$ -axis positions of the surface and of the end-effector, respectively,  $d = z_{\text{surf}} - z_{\text{EE}}$  by definition,  $F_{\text{unc}}$  is the rated uncertainty of the sensor and  $F$  is the measured force. This way, it is possible to find the position of the surface with precision despite the uncertainties of the force sensor, while at the same time estimating the elastic modulus  $E_f$ .

## III. ONLINE VISCOELASTICITY ESTIMATION PROCESS

This section presents an online algorithm that estimates penetration, penetration rate, elasticity, and viscosity by modelling the contact between a spherical indenter and a soft material using an Extended Kalman Filter (EKF).

### A. Point Estimation

To simplify the formulation of the force generated by a spherical indenter presented in (12), two new parameters have been defined:

$$\kappa = \frac{4}{3} \frac{E_f}{1-\nu^2} \sqrt{R} \quad \text{and} \quad \lambda = \frac{4}{1-\nu} \eta \sqrt{R}, \quad (15)$$

obtaining a new formulation of the total force (12) as

$$F_{DR}(d) = \begin{cases} \kappa d^{\frac{3}{2}} + \lambda d^{\frac{1}{2}} \dot{d}, & d \geq 0, \\ 0 & d < 0. \end{cases} \quad (16)$$

A dynamical system can be obtained to describe the evolution of the contact between the indenter and the soft surface given in (16). First, we define the state vector  $\mathbf{x} = [d, \dot{d}, \kappa, \lambda]$ , describing the amount of penetration  $d$ , the penetration rate  $\dot{d}$ , the normalised elasticity  $\kappa$  and the normalised viscosity  $\lambda$ . With  $\Delta T$  being the sampling time of the dynamic model and denoting with  $x_{i,t}$  the  $i$ -th variable of  $\mathbf{x}$  at time instant



$t\Delta T$ , the discrete-time system dynamics  $\mathbf{x}_{t+1} = f_t(\mathbf{x}_t, u_t, \mathbf{w})$  describing (16) is then given by

$$\begin{aligned} x_{1,t+1} &= x_{1,t} + \Delta T x_{2,t} + \\ &\quad \frac{\Delta T^2}{2m_I} \left( u_t - x_{1,t}^{\frac{3}{2}} x_{3,t} - x_{1,t}^{\frac{1}{2}} x_{2,t} x_{4,t} \right) + w_{1,t}, \\ x_{2,t+1} &= x_{2,t} + \frac{\Delta T}{m_I} \left( u_t - x_{1,t}^{\frac{3}{2}} x_{3,t} - x_{1,t}^{\frac{1}{2}} x_{2,t} x_{4,t} \right) + w_{2,t}, \\ x_{3,t+1} &= x_{3,t}, \\ x_{4,t+1} &= x_{4,t}. \end{aligned} \quad (17)$$

The input  $u_t$  is the force registered by a force-torque sensor along the direction perpendicular to the surface, while  $\mathbf{w}_t = [w_{1,t}, w_{2,t}]^T$  is the i.i.d., zero mean, Gaussian process model of the uncertainties, namely  $\mathbf{w}_t \sim \mathcal{N}(\mathbf{0}, \mathbf{Q})$ . The input  $u$  gives the uncertainty of the measurement model, the force measured by the F/T sensor. The process noise  $\mathbf{w}_t$  can be written as a function of the standard deviation  $\sigma_u$  of the input force  $u$ .  $\sigma_u$  can be considered a time-invariant quantity, as it remains constant throughout the experiment. The standard deviations of the penetration and the velocity can be computed as follows:

$$\sigma_{x_1} = \frac{\Delta T^2}{2m_I} \sigma_u \quad \text{and} \quad \sigma_{x_2} = \frac{\Delta T}{m_I} \sigma_u. \quad (18)$$

Said  $\mathbf{B} = \begin{bmatrix} \frac{\Delta T^2}{2m_I} & \frac{\Delta T}{m_I} \end{bmatrix}^T$ , the covariance matrix  $\mathbf{Q}$  of the uncertainties  $\mathbf{w}_t$  can then be defined as

$$\mathbf{Q} = \mathbf{B} \sigma_u^2 \mathbf{B}^T. \quad (19)$$

The measurement function  $z_t = h(\mathbf{x}_t, v_t)$  is instead the velocity of the end effector in the direction orthogonal to the surface, i.e.

$$z_t = x_{2,t} + v_t, \quad (20)$$

where  $v_t$  is the i.i.d zero mean Gaussian process generating the velocity measurement uncertainty,  $v_t \sim \mathcal{N}(0, \sigma_{vel}^2)$ , which is the only uncertainty contribution here.

Using the knowledge of the model of the system  $f_t(\mathbf{x}_t, u_t, \mathbf{w}_t)$ , its input measurements  $u_t$  and the stochastic description of the associated uncertainties  $\mathbf{w}_t$ , together with the velocity measurements  $h(\mathbf{x}_t, v_t)$ , an EKF is employed to derive the contact properties (penetration extent and velocity, elasticity and viscosity) estimates. Similar to what was done in [18], [20], the palpation will be simulated by a sinusoidal motion perpendicular to the soft surface. In the interest of space, the EKF equations are not reported in this manuscript, but a similar implementation can be found in our previous report [30].

### B. Dynamic Estimation

Although point estimation is a useful method for measuring specific properties, it is not a practical approach for mapping the stiffness variation of a material, since an extensive number of measurement points would be needed. Moreover, during a point estimation, elasticity and stiffness remain constant throughout the measurement phase, which is no longer the case for dynamic estimation. In other words, the value at which the EKF based on (17) converge for those parameters, which

are supposed to be constant due to a lack of model information, actually change dynamically. Therefore, to increase the expressivity of the model presented in Section III-A, the system described in (17) is expanded with a dynamic term for the elasticity and viscosity values. More in depth, we redefine the state as  $\mathbf{x} \in \mathbb{R}^8$ , with  $\mathbf{x} = [d, \dot{d}, \kappa, \lambda, \dot{\kappa}, \dot{\lambda}, \ddot{\kappa}, \ddot{\lambda}]$ , whose dimension is twice as much as the one in (17). Incorporating second-order derivatives as state variables is an effective strategy for accelerating convergence, particularly in scenarios characterized by rapid variations in viscoelastic parameters. This capability proves especially significant in real-time safety-critical applications, such as physical human-robot interaction, where accurate estimation of viscoelastic parameters enables precise prediction of interaction forces exerted on a patient's body, tailored to the specific anatomical location involved. The new discrete-time model will then be

$$\begin{aligned} x_{1,t+1} &= x_{1,t} + \Delta T x_{2,t} + \\ &\quad \frac{\Delta T^2}{2m_I} \left( u_t - x_{1,t}^{\frac{3}{2}} x_{3,t} - x_{1,t}^{\frac{1}{2}} x_{2,t} x_{4,t} \right) + w_1, \\ x_{2,t+1} &= x_{2,t} + \frac{\Delta T}{m_I} \left( u_t - x_{1,t}^{\frac{3}{2}} x_{3,t} - x_{1,t}^{\frac{1}{2}} x_{2,t} x_{4,t} \right) + w_2, \\ x_{3,t+1} &= x_{3,t} + \Delta T x_{5,t} + \frac{\Delta T^2}{2} x_{7,t}, \\ x_{4,t+1} &= x_{4,t} + \Delta T x_{6,t} + \frac{\Delta T^2}{2} x_{8,t}, \\ x_{5,t+1} &= x_{5,t} + \Delta T x_{7,t}, \\ x_{6,t+1} &= x_{6,t} + \Delta T x_{8,t}, \\ x_{7,t+1} &= x_{7,t}, \\ x_{8,t+1} &= x_{8,t}, \end{aligned} \quad (21)$$

which is adopted as the model for the prediction step of the EKF.

However, the dynamics considered for the elasticity and viscosity (i.e., the last six variables in (21)) model a second-order system, which cannot account for abrupt changes, as instead happens in presence of a mass in the body. Therefore, to make the EKF more prompt and, hence, detect such rapid changes, we use as a detection metric the *likelihood* between the estimated model and the measurements. This entails defining an inflating fudge factor  $\alpha \in [1, \alpha_{\max}]$ , which multiplies the filter covariance matrix [31]. In instances where the error exceeds a specified threshold  $\theta$ ,  $\alpha$  increases; conversely, it decreases. The increment and decrement are defined as  $\Delta\alpha$ , in the experimental section we will see the effect of varying this value. Letting  $\bar{y}_t = z_t - h(\bar{\mathbf{x}}_{t|t-1})$  be the innovation, where  $\bar{\mathbf{x}}_{t|t-1}$  is the predict state, the updating rule of  $\alpha$  is:

- 1) Calculate the magnitude of the innovation  $\bar{y}_t$
- 2) Update the fading factor  $\alpha$  based on the magnitude of the innovation:

$$\alpha = \begin{cases} \min(\alpha_{\max}, \alpha + \Delta\alpha), & \text{if } \bar{y}_t > \theta; \\ \max(1, \alpha - \Delta\alpha), & \text{otherwise.} \end{cases}$$

- 3) Correct the predicted covariance of the estimates as

$$\mathbf{P}_{t|t-1} = \alpha \mathbf{P}_{t|t-1}.$$

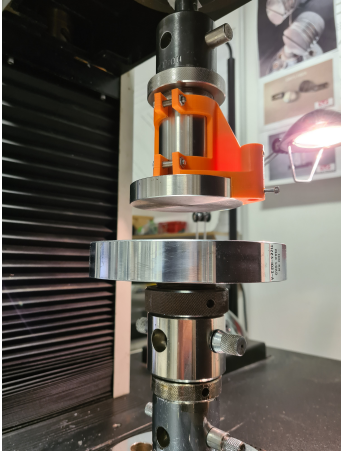


Fig. 4. Instron® 4502 dynamometer used for the ground truth collection of the specimens characteristics.

Increasing the fading factor  $\alpha_{max}$  will decrease the low pass effect of the filter, decreasing the delay of the estimation process but increasing the uncertainties. On the other hand, increasing the threshold  $\theta$  will have the opposite effect.

The procedure for dynamic palpation is divided into two distinct steps. In the initial phase, sinusoidal palpation is conducted in a direction perpendicular to the surface of the material, with no movement along the other axes. This is done to allow the filter sufficient time to converge to the appropriate values of the states. In the subsequent phase, sinusoidal palpation continues, but movement in a direction of interest is also introduced. Notice that different speeds of the end-effector may have different effects on the elasticity estimates, therefore this aspect should be carefully investigated.

#### IV. EXPERIMENTAL SETUP

The measurement system was characterized using a set of specimens whose properties were determined with a reference instrument for compression testing, serving as the ground truth. Specifically, quasi-static compression tests were conducted at 23°C using an Instron® 4502 dynamometer (Norwood, MA, USA) equipped with a 50 kN load cell, as shown in Fig. Fig. 4. During the tests, the cross-head speed was of 50 mm/min and the sampling rate of the dynamometer was of 25 pt/s (or 25 Hz) up to 5 mm of compression.

##### A. Robotic system

The experimental setup includes an Ur3e, a widely used collaborative 6 degree-of-freedom robotic arm. It has a maximum payload of 3 kg and a pose repeatability per ISO 9283 of  $\pm 0.03$  mm. It operates at 500 Hz. At the end-effector of the manipulator, it is attached a 6-axis force-torque sensor, i.e., the BOTA System SensONE. The sensor works at 1 kHz with standard deviation of the signal over 1 second of measurements in stable conditions of 0.05 N in the  $z$ -direction. After a warm-up phase, the measurements can be considered uncorrelated since there is a drift of less than 1.5 N/h and our experiments have a maximum duration of 40 seconds. Attached to the sensor there is a 3D printed indenter. The

robotic arm is controlled by a simple motion controller in the Cartesian space. Hence, given the Cartesian position of the end-effector as input, the values of the joints are calculated by the robot inverse kinematics. A PD controller regulates the convergence speed, with the proportional gain empirically set to 20 and the derivative gain to 0.5, ensuring that the end-effector follows the trajectory with negligible error (i.e., below one millimeter)..

##### B. Data Acquisition Protocol

End-effector position and velocity data are obtained from the robot encoders using forward kinematics based on the Denavit-Hartenberg convention [32]. With these rules, it is possible to obtain a homogeneous transformation matrix for each of the  $m$  joints as

$$T_i = \begin{bmatrix} R_i & p_i \\ 0 & 1 \end{bmatrix}, \quad (22)$$

where  $i$  is the joint number,  $R_i \in \mathbb{R}^{3 \times 3}$  is the orientation matrix representing the orientation of the joint  $i$  and  $p_i \in \mathbb{R}^{3 \times 1}$  is the position of the joint  $i$ . The pose of the end effector for the  $m = 6$  joint arm can then be expressed as the product of the  $m$  transformations in (22), i.e.,

$$T_{ee} = T_1 T_2 \cdots T_m. \quad (23)$$

Similarly, it is possible to use the Jacobian matrix to obtain, from the robot joint velocities, and the end effector velocities. While position values are used within the offline estimation (14), speed values are used within the filter measurement function (20). In the proposed EKF, the position, velocity, and acceleration data are expressed in millimeters to avoid numerical errors, induced by the significant difference in orders of magnitude between stiffness and damping, that may impair the convergence of the filter. The force data  $u_t$  are collected directly from the force-torque sensor mounted on the robot end-effector. They are used both for the minimisation problem (12) and as input for the filter prediction step using (21). Using (18) and the value of the standard deviation of the force sensor along the  $z$  axis, it is possible to derive the model uncertainties  $\sigma_{x_1}^2 = 1.12 \times 10^{-6}$  mm  $\sigma_{x_2}^2 = 0.3044$  mm/s using a Type B [33] derivation using (18).

Instead, the mass of the portion of the end effector that is placed after the F/T sensor and in contact with the body has been estimated by comparing the inertia of the system with the measured force during a sinusoidal motion and using a least squares approach. Finally, the standard uncertainty on the velocity  $\sigma_{vel}$  has been derived by imposing on the robot end effector a sinusoidal motion along the  $z$ -axis and then recording its cartesian velocity with a sampling time of 2 ms. Using a moving average filter of 21 consecutive samples, the root mean squared error between the filtered and measured velocities is computed. This procedure has been done 3 times and, since the measurements had a negligible bias and the sequence correlation in the time window of the experiments was again negligible, we obtained a variance for the velocity measurements equal to  $\bar{\sigma}_{vel}^2 = 0.4489$  mm/s.

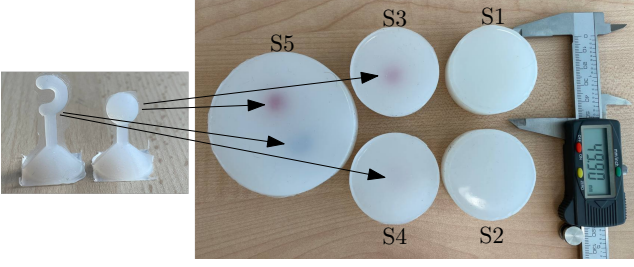


Fig. 5. On the right are shown the cylindrical silicones used during the experiments, while on the left are the spherical and horseshoe-shaped intrusions.

### C. Specimens

Silicone specimens were used in this study due to their similarity to biological tissues [34], specifically ECOFLEX-0030, Dragonskin-10NV, and Dragonskin-30, listed from softest to hardest. The specimens tested in the point-based experiments were cylinders with a diameter of 50 mm and a height of 22 mm. Spherical and horseshoe-shaped inclusions were embedded in two samples made from the softer matrix to simulate stiffer cancerous tissue within softer, healthy tissue, as in [35]. Listed below are the specimens used with their relative abbreviations:

- **S1:** Dragonskin-10NV matrix,
- **S2:** ECOFLEX-0030 matrix,
- **S3:** ECOFLEX-0030 matrix and Dragonskin-30 horseshoe intrusion,
- **S4:** ECOFLEX-0030 matrix and Dragonskin-30 spherical intrusion.

Finally, a bigger sample (**S5**), with diameter 80 mm, containing both a spherical and horseshoe intrusion has been used for the dynamic experiments. Specimens and intrusions are shown in Fig. 5. We assumed the silicon samples, considering them incompressible, with a  $\nu = 0.5$ . This is a broadly accepted assumption, which comes from experimental evidence and is used in the vast majority of works dealing with continuum mechanics of rubber-like materials [34], [36].

## V. ELASTIC MODULUS ESTIMATION PROCESS

Experiments to estimate the elastic modulus with the UR3e manipulator were conducted with three different tips: a flat tip with 5 mm radius, a spherical tip with 5 mm radius and a quartic surface with  $c_4 = 10^7$  (see(9)), all shown in Fig. 6. To compare the different tips, the penetration velocity remained consistent at 50 mm per minute. The indentation depth is adjusted to 10% of the sample thickness to stay within the range of material linearity [37], since any deeper penetration could amplify the non-linear characteristics of the material that are not modelled. During the experiment, the position and the force in the  $z$ -direction is collected for post-processing, while 14 is used to estimate the elasticity modulus.

Fig. 7 shows the mean error between the reconstructed force using, respectively, the models in (5), (8) and (9), and the measurement force acquired by the F/T Sensor. More precisely

$$e_i = F_{\text{EST},i} - F_{\text{FT},i}, \quad (24)$$



Fig. 6. 3D-printed tips utilised in the experiments. From left: the flat, the quartic and the spherical tips.

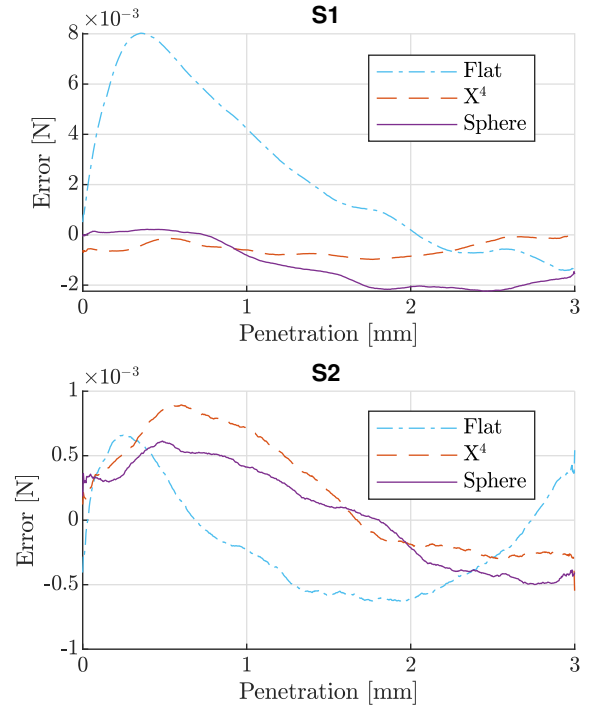


Fig. 7. Average force error between the measured and the estimated value in the S1 and S2 specimens.

where  $i$  is the  $i$ -th test,  $F_{\text{FT}}$  is the measured force and  $F_{\text{EST}}$  is the estimated force with the different models. The discrepancy is consistently minimal, except for the flat indenter with the hardest silicone. The considerable initial discrepancy, which is not discernible in the graph of the softer silicone, can be attributed to the fact that the surfaces are not perfectly parallel, resulting in a non-linear effect of force until complete contact is achieved.

The estimated elasticity quantities are consistent with the ground truth, as depicted in Table I. The flat tip exhibits the poorest behaviour with a maximum relative error of nearly 20%, with a big difference between S1 and S2. This could be, again, caused by the alignment imperfections between the indenter. The estimates provided by the quartic indenter exhibits a consistent error of approximately 10% for both specimens. In contrast, the spherical indenter exhibits the smallest error, with a value below 5%.

TABLE I

RESULTS OF THE ELASTIC MODULUS ESTIMATIONS OF **S1** AND **S2** USING THE THREE TIPS OF DIFFERENT SHAPE, WITH 50 TESTS EACH.  $\mu$  IS THE ELASTIC MODULUS,  $\sigma$  IS THE STANDARD UNCERTAINTY, AND Error THE RELATIVE ERROR WITH RESPECT TO THE GROUND TRUTH.

	GROUND TRUTH		FLAT TIP			QUARTIC TIP			SPHERICAL TIP		
	$\mu$ [kPa]	$\sigma$ [kPa]	$\mu$ [kPa]	$\sigma$ [kPa]	Error [%]	$\mu$ [kPa]	$\sigma$ [kPa]	Error [%]	$\mu$ [kPa]	$\sigma$ [kPa]	Error [%]
<b>S1</b>	282.1	0.3	302.3	0.7	7.9	311.0	2.1	11.07	283.9	0.9	1.4
<b>S2</b>	112.5	0.2	131.7	0.6	17.6	122.1	0.4	8.9	117.5	0.5	4.9

## VI. VISCOELASTICITY EXPERIMENTS

We start this section by experimentally comparing the chosen DR model presented in Section II with the two most widely adopted alternatives in robotics, which are typically employed to represent contact behaviours with soft bodies. The first is the Kelvin-Voigt (KV) model, which is used for its simple linear representation that ensures the contact forces description with a relatively minimal degree of error. It is described by

$$F_{KV}(d) = \begin{cases} Kd + B\dot{d}, & d \geq 0, \\ 0, & d < 0, \end{cases} \quad (25)$$

where  $K$  is the stiffness and  $B$  is the damping related to the spring-damper system. The second is the Hunt-Crossley (HC) model described by

$$F_{HC}(d) = \begin{cases} K_c d^n + B_c d^n \dot{d}, & d \geq 0, \\ 0, & d < 0, \end{cases} \quad (26)$$

where  $K_c$  is the stiffness,  $B_c$  is the damping and  $n$  is a parameter dependent on the type of contact [16]. This non-linear model is capable of faithfully reconstructing the contact force and does and widely reduces the representation error of (25). The HC model also has the advantage of not being defined for any specific shape of the contact surface. This flexibility comes with a main drawback: the coefficient  $n$  in (26) must be estimated online, which makes the estimation process more challenging. Another disadvantage is the absence of a direct relationship between the stiffness and the elasticity modulus of the material, and between the damping value and the viscosity modulus.

A load test was conducted to evaluate the performance of the three models (KV, HC and DR) under varying indentation speeds. This test involved a load and unload phase at a constant speed. In this phase, the elasticity and viscosity parameters, including the exponent  $n$  of the HC model in (26), are computed offline using a least squares minimisation. Fig. 8 shows the result of these minimisations. The evolution of the error  $e_i$  computed as in (24), is shown in Fig. 9. As anticipated, the KV model is suitable whenever an accurate force reconstruction is not needed. This model does not take into account the variations of the contact surface during indentation. Its load cycle is also energetically inconsistent [19], as the force does not start and end at zero since the contact velocity is not zero. Both the HC and the DR method turn to be effective for the force representation. The HC model presents an additional

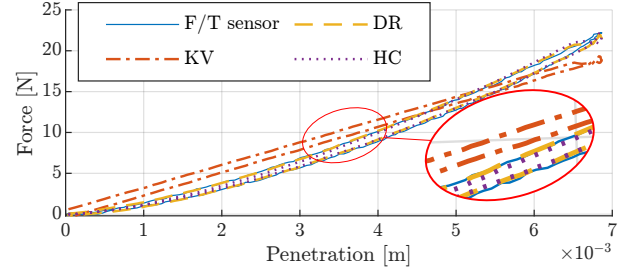


Fig. 8. Reconstruction of the force of the load tests using the 3 KV, HC and DR models.  $n = 1.53$  is estimated for the HC.

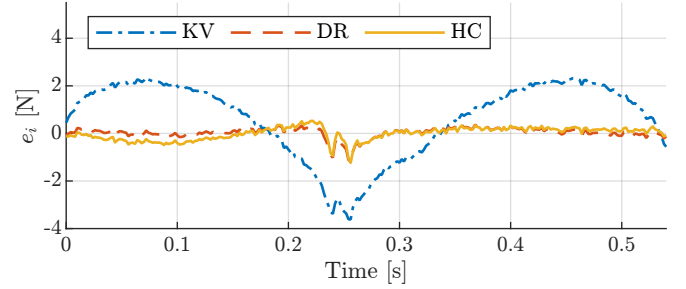


Fig. 9. Error between the force measurements and the force computed by the contact models.

layer of complexity due to the nonlinearity of the unknown exponent that has to be estimated online during the estimation. For a quantitative comparison, the residual values of the least squares are reported in Table II. It can be observed that, despite the residual errors of the HC and DR models are similar, the latter exhibits smaller errors (see Fig. 9).

The residuals with different indentation speeds have been also computed and reported in Table III, adopting the elasticity and viscosity values obtained from the previous test. This additional check was performed to ensure that no overfitting in the first load cycle data is present. It is possible to observe that the results obtained with the initial tests at speed  $v_0 = 6$  mm/s match the tests at speeds  $v_1 = 4$  mm/s and  $v_2 = 8$  mm/s, proving that the adopted models are correct. The experimental evidence shows that the adopted DR model is the best fit for the problem at hand.

### A. Online Point Estimation

We report here on the online point estimation carried out with an EKF based on the DR model of (17) and (20), and used to estimate the elasticity and viscosity online. At the



TABLE II  
RESIDUALS RESULTING FROM THE LEAST-SQUARES MINIMISATION  
PROCESS EMPLOYED TO ESTIMATE THE PARAMETERS DERIVED FROM THE  
LOAD TESTS.

RESIDUAL VALUE [N <sup>2</sup> ]		
Kelvin-Voight	Dimensionality-Reduction	Hunt-Crossley $\beta = 1.53$
792.45	13.62	20.59

TABLE III  
RESIDUALS WITH VARYING INDENTATION SPEED.

RESIDUAL VALUE [N <sup>2</sup> ]		
Velocity	Dimensionality-Reduction	Hunt-Crossley $\beta = 1.53$
$v_0$	13.62	20.59
$v_1$	20.18	32.08
$v_2$	20.14	23.75

end-effector is imposed a sinusoidal motion along the  $z$ -axis, which is perpendicular to the sample and equal to

$$z(t) = z_0 + z_a \sin(2\pi\omega t), \quad (27)$$

where  $z_0$  is the bias inside the sample, i.e., the initial penetration,  $z_a$  is the amplitude of the sinusoid, and  $\omega = 2$  Hz is the frequency of the palpation. The selection of palpation frequency constitutes a trade-off between the limitation of robot dynamic properties, the precision of elasticity estimation, and viscosity estimation. Frequencies that are excessively high result in the estimation of erroneous elasticity values, while frequencies that are insufficiently low preclude the estimation of the viscous properties of the material. The EKF starts when the indenter is in contact with the surface.  $z_0$  was set to 2 mm for the smallest tip and to 4 mm for the other two tips, while  $z_a$  was set to 1 mm regardless of the tip shape. These choices ensure motion in the linear elastic regime of the samples, since a bigger penetration would cause the bulging of the lateral surface. The filter based on (17) is initialised with an initial state  $x_0 = [1, v_0, 0.1, 0.01]$ , where 1 mm is the initial guess of the penetration,  $v_0$  is the initial velocity along the  $z$ -axis measured by the robot, 0.1 is the initial guess on  $\kappa$  and 0.01 on  $\lambda$ . The covariance matrix  $P$  of the EKF is initialised as a diagonal matrix  $P = \text{diag}([5, 1, 1, 1])$ , whose values have been tuned through experimental tests.

1) *Estimates Correlation*: To ensure that the elasticity of the sample does not change along the experiment execution due to the relaxation effect (i.e., the effect that changes the viscoelastic characteristics of a material after an excitation),  $n = 100$  measurements were taken for the hard **S1** and soft **S2** silicone samples and reported in Fig. 10 with a histogram. We then computed the correlation coefficients  $\rho_{S1} = 0.19$  and  $\rho_{S2} = -0.45$  for the hard and soft silicone, respectively, which substantiates the existence of a slight correlation between the data of the hard silicone and soft silicon. Those values are clearly shown in the autocorrelation function plot of Fig. 11. To further investigate this trend, we calculated the moving average using a sliding window. We utilise a window size

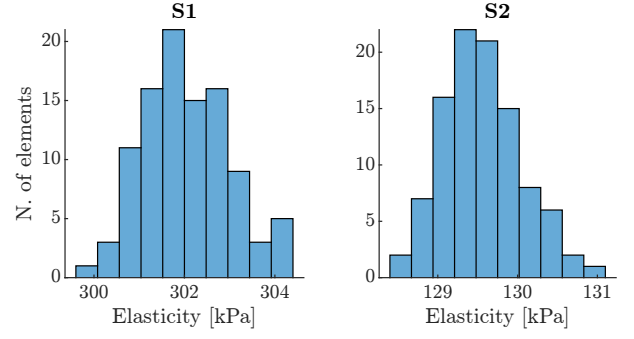


Fig. 10. Histogram of the elasticity measurements of the hard **S1** and soft **S2** silicone samples.

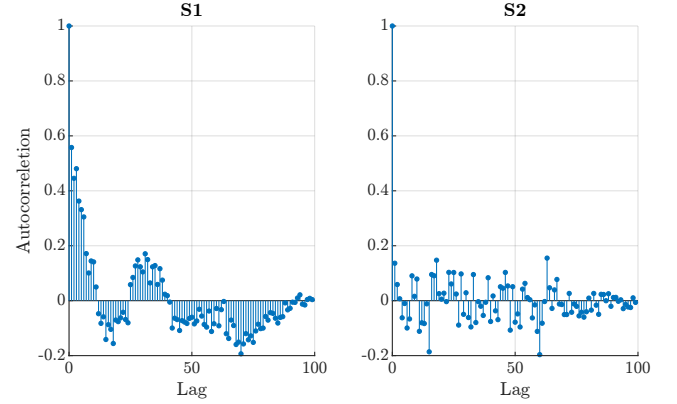


Fig. 11. Autocorrelation function of the elasticity measurements of the hard **S1** and soft **S2** silicone samples.

of 30 values, which smoothes out short-term fluctuations and highlights longer-term trends. From Fig. 12, it can be seen that there is a slight decrease for S1 and increase for S2 in the stiffness when the number of measurements increases. For our experiments, this effect is deemed to be negligible.

2) *Elastic modulus estimate Validation*: The aim here is to perform a comparison between the online estimate of the elastic modulus and the value obtained through a compression test performed with the dynamometer Instron® 4502 described in Section IV and depicted in Fig. 4, whose measurements are considered as ground truth. The detailed procedure to obtain such quantities is described in Appendix A. To investigate the impact of varying tip diameter on estimation accuracy, three spherical tips with diameters  $r$  of 4 mm, 10 mm and 20 mm were adopted. For each tip, 50 measurements were obtained and filtered with the EKF (17) and then compared with 10 measurements taken with the compression test. Table IV collects the results of the tests thus described: the  $r = 2$  mm tips yielded accurate elasticity estimates for both the soft and hard samples. Increasing the size of the tip also increases the error in the estimate. This phenomenon can be attributed to the DR model's assumption of infinite flat surface contact, which fails to account for the potential effects that may arise when this assumption is invalid. Notably, the effects are limited and consistent for both silicones as long as the tip radius is not excessively large, i.e., 5 mm. However, when employing a 10 mm tip, these effects become too invasive, and the estimate

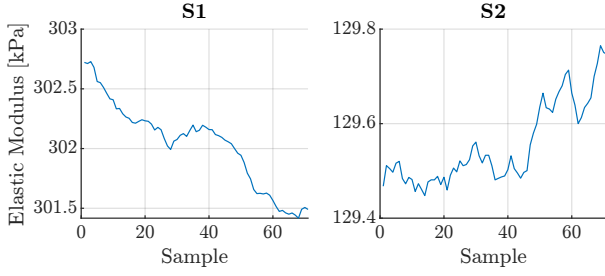


Fig. 12. Moving average of the elasticity measurements for the hard **S1** and soft **S2** silicone samples with a sliding window of 30 elements.

becomes invalid.

However, one can consider using a 5mm radius tip despite the absolute error in elasticity estimation because in a scouting setup it covers a larger area and is therefore more likely to provide useful information than a very small tip such as the 2mm radius tip.

3) *Viscosity Validation*: As the compression tests were conducted with the dynamometer in Section IV which performs quasi-static tests, it is not possible to extrapolate the viscous values of the silicone specimens. Consequently, we relatively compare the viscosity values obtained through the online estimation process among them with different spherical tip radii. The viscosity estimates, collected in Table V, reveals that the 2.5 mm and 5 mm radius tips are highly similar, whereas those for the 10 mm tips are quite different, thus confirming the test outputs collected in Table IV. Hence, from this point on the rest of the experiments will be conducted with the  $r = 5$  mm spherical indenter.

4) *Lump Detection*: The point online estimation was then used to identify the viscoelastic parameters of specimens containing harder silicone parts, as in cancer detection palpation tests. Hence, the objective of this experimental study was to see if there is a change in stiffness and if this change is significant enough to be used in a detection process. Table VI reports the results of these experiments: both harder insertions can be detected by looking at the mean  $\mu$  of the elasticity values. The statistical analysis, conducted using the Student's t-test, confirmed that the differences in tumour detection results were highly significant, with p-values falling well below the 0.01 threshold. Moreover, the low standard deviation exhibited in these experiments opens to an efficient detection process.

### B. Online Dynamic Estimation

The transition from point to dynamic palpation increases the efficacy and speed of the analysis but presents a more challenging estimation scheme since the indenter tip now has to slide on the surface while ensuring a continuous palpation with desired contact forces. In order to test the effectiveness of this new dynamic scheme, the results are compared with the point estimation approach of subsection VI-A when the estimation points are chosen sufficiently close to each other and, hence, resulting in a sampling based ground truth for the dynamic estimators at hand. The additional variables of the dynamic estimators in  $\mathbf{x}_0$ , which is adopted in (21), are initialised to zero since at the beginning the elasticity

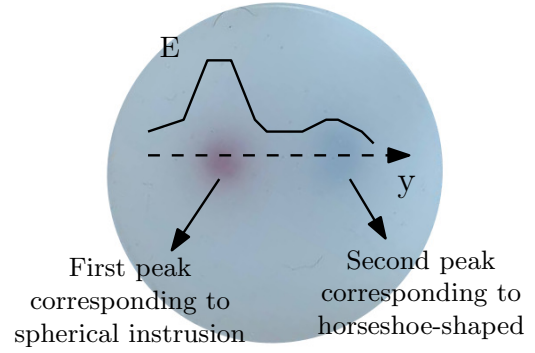


Fig. 13. Trajectory ( $y$ ) of the robot end effector on the silicon sample containing the spherical and horse-shaped intrusions.

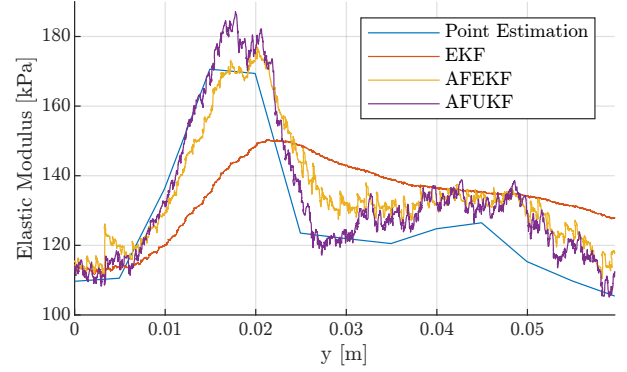


Fig. 14. Dynamic elasticity estimation using the three different filters adopted, i.e., EKF, AFEKF, and AFUKF, with a comparison with the point estimation, which is made by sampling the silicone once every 5 mm (that is, the indenter radius). The two picks in the figure refer to the sphere and the horseshoe beneath the silicone surface.

and viscosity parameters will be constant with a covariance of  $\text{diag}(\mathbf{P}) = [5, 1, 1, 1, 0.1, 0.1, 0.1, 0.1]$ . The **S5** specimen was employed in these experiments: as discussed in subsection IV-C, this specimen has two embedded intrusions, one is a sphere and the other one a horseshoe (see Fig. 5 and Fig. 13). The continuous test starts with a 10 second point palpation, as in the previous test, and then progresses in a predetermined direction at a constant speed. The outcomes of the continuous palpation are illustrated in Fig. 14.

Here, the continuous estimation is performed employing three different filtering techniques: a) the EKF presented previously, to see how the estimation works without any improvement; b) the Adaptive Fading Extended Kalman Filter (AFEKF) [38], which adopt a forgetting factor on the covariance matrix computation to account for modelling uncertainties in this parameter; c) the Adaptive Fading Unscented Kalman Filter (AFUKF) [39] that uses the expanded state and a fading scheme similar to the AFEKF but applied to the Unscented Kalman Filter (UKF). The fading factors  $\theta$  and  $\alpha$  adopted in filters have been discussed in detail in subsection III-B. Therefore, the three compared solutions are:

- The EKF using equations (17) and (20);
- The AFEKF using again equations (17) and (20);
- The AFUKF using the expanded state in (21) and the

TABLE IV

RESULTS OF THE ELASTIC MODULUS ESTIMATIONS OF **S1** AND **S2** USING THE THREE SPHERICAL TIPS ALONG 50 TESTS EACH.  $\mu$  IS THE MEAN VALUE OF THE ELASTICITY,  $\sigma$  IS THE STANDARD UNCERTAINTY, AND Error THE RELATIVE ERROR WITH RESPECT TO THE GROUND TRUTH (I.E., THE 10 AVERAGED DYNAMOMETER MEASUREMENTS).

	GROUND TRUTH		SPHERICAL TIP $r = 2$ mm			SPHERICAL TIP $r = 5$ mm			SPHERICAL TIP $r = 10$ mm		
	$\mu$ [kPa]	$\sigma$ [kPa]	$\mu$ [kPa]	$\sigma$ [kPa]	Error [%]	$\mu$ [kPa]	$\sigma$ [kPa]	Error [%]	$\mu$ [kPa]	$\sigma$ [kPa]	Error [%]
<b>S1</b>	282	0.3	276.8	1.4	1.8	302.4	0.8	7.2	377.1	1.3	33
<b>S2</b>	112	0.2	109.7	1.1	2.2	129.5	0.5	15.7	175.8	0.8	57

TABLE V

COMPARISONS OF THE AVERAGE  $\mu$  AND THE STANDARD DEVIATION  $\sigma$  OF THE VISCOSITY ESTIMATES FOR **S1** AND **S2** SAMPLES WITH A SPHERICAL TIP OF DIFFERENT RADII.

Sample	VISCOSITY ESTIMATES [Ps]					
	$r = 2$ mm		$r = 5$ mm		$r = 10$ mm	
	$\mu$	$\sigma$	$\mu$	$\sigma$	$\mu$	$\sigma$
<b>S1</b>	1028	36	860	35	1000	33
<b>S2</b>	517	25	362	14	444	16

TABLE VI

COMPARISONS OF THE AVERAGE  $\mu$  AND THE STANDARD DEVIATION  $\sigma$  OF THE ELASTICITY AND VISCOSITY ESTIMATES FOR THE MODIFIED SPECIMENS **S3** AND **S4**, DESCRIBED IN SECTION IV-C AND COMPARED TO THE VALUE WITHOUT HARD INSERTIONS.

Modulus	ELASTICITY AND VISCOSITY ESTIMATES					
	<b>S2</b>		<b>S3</b>		<b>S4</b>	
	$\mu$	$\sigma$	$\mu$	$\sigma$	$\mu$	$\sigma$
Elasticity [kPa]	129.5	0.7	142.8	0.7	171.4	1.0
Viscosity [Pas]	362	16	399	16	458	16

measurement function in (20).

A comparison has been made between the elasticity estimation of the three models and the punctual palpation performed with 5 mm intervals, which is equal to the radius of the indenter. It is expected that two elasticity picks are detected: the first when the harder silicone sphere is encountered beneath the surface; the second for the horseshoe. From Fig. 14, the EKF cannot estimate the correct values due to the slow convergence rate, while the AFEKF accurately estimates the elasticity values but still exhibits a slight delay. The AKUKF eliminates the delay in estimation but introduces greater oscillation and a larger overshoot when the indenter encounters a stiffer region. Both the filters that use the adapting fading factor can identify two picks, with the second being more pronounced in the UKF case.

To further investigate the impact of the fading factor on the best performing AKUKF dynamic estimation algorithm, Fig. 15 presents a performance comparison when the fading factors  $\theta$  and  $\alpha$  change. With an increased value of  $\theta$  and lower of  $\alpha$ , the estimates are smoother but the responsiveness is reduced. Conversely, reducing  $\theta$ , the filter is more responsive but the estimation exhibits significant uncertainty. Consequently, a compromise between these two behaviours

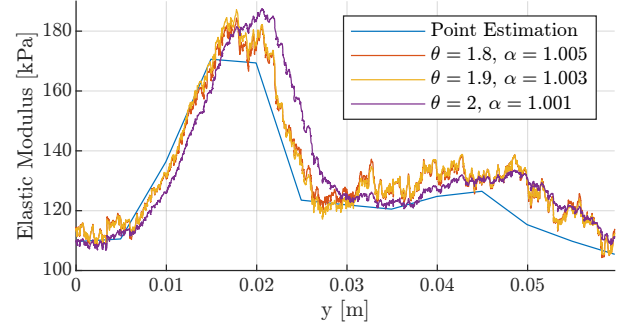


Fig. 15. Effect of varying fading values  $\theta$  and  $\alpha$  on the elasticity estimates compared, with a comparison with the point estimation.

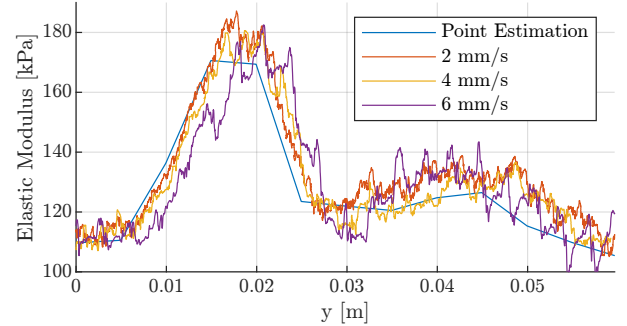


Fig. 16. Effect of indenter velocity (in mm/s) on the elasticity estimates, again compared with the point estimation.

can be determined by direct calibration. Moreover, the AFUKF was tested with varying indenter velocities to determine how the estimation performance would change. The results are reported in Fig. 16. It was found that both the 2 mm/s and 4 mm/s velocities showed good performance and a high degree of similarity, while the 6 mm/s velocity had an increased estimation uncertainty.

### C. Preliminary Test on Ex Vivo Biological Tissue

To provide a preliminary evaluation of the method on biological tissue, we conducted a proof-of-concept ex vivo experiment with chicken breast [37], [40]. The aim of this test is to extend the results with silicones to biological sample, assessing the system ability to estimate the viscoelastic properties of soft biological material, both in the presence and absence of a stiffer inclusion, which was created by inserting a 5 mm-diameter silicone sphere made of DragonSkin-30,



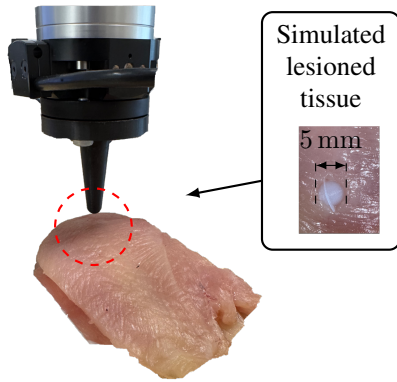


Fig. 17. Proof-of-concept experiment with chicken breast. On the right, it is possible to see the silicon sphere used to simulate the damaged tissue during the viscoelasticity estimation.

TABLE VII  
ESTIMATED VISCOELASTIC PROPERTIES (MEAN AND STANDARD DEVIATION) OF EX VIVO CHICKEN BREAST SAMPLES WITH AND WITHOUT A STIFFER SILICONE INCLUSION OVER 10 REPEATED PALPATIONS.

ELASTICITY AND VISCOSITY ESTIMATES				
Modulus	Chicken Breast		Chicken Breast with Sphere	
	$\mu$	$\sigma$	$\mu$	$\sigma$
Elasticity [kPa]	53.7	5.2	102.7	10.7
Viscosity [Pa s]	623	101	1095	150

identical to the one used in the S4 scenario, between two chicken breast slices, each approximately 15 mm thick. To accommodate the sphere, a slot was cut into the upper surface of the lower slice using a scalpel, as shown in Fig. 17. In the first trial, the robot palpated the tissue without any inclusion to establish baseline viscoelastic properties. In the second trial, the silicone sphere was inserted between the slices to simulate the presence of a stiffer lesion within soft tissue.

The results, summarised in Table VII, show a clear difference between the two conditions. The presence of the stiffer inclusion resulted in a noticeable increase in both estimated elasticity and viscosity. These findings indicate that the proposed method can effectively detect and localise mechanical anomalies, such as stiffer inclusions, within biological tissue. The higher standard deviations observed in this experiment, compared to those obtained with homogeneous silicone samples VI-A2, VI-A3, VI, highlight the natural variability of biological materials and the challenges in maintaining consistent contact conditions across repeated measurements.

Despite these non-ideal measurement conditions, the results demonstrate promising potential for clinical applications, particularly in identifying and localising stiffer regions within soft tissue, such as tumours or fibrotic areas. The method's ability to estimate viscoelastic properties through robotic palpation offers valuable diagnostic support, especially in contexts where visual feedback is limited, such as minimally invasive or robot-assisted procedures. Although preliminary, the successful application to ex vivo tissue confirms the feasibility of using the method on biological material and lays the groundwork for future integration into clinical studies.

## VII. CONCLUSION

An method to estimate the viscoelastic parameters of a soft material using a robotic arm has been presented. This is relevant to the development of robotic medical applications based on the physical interaction between a probe and the patient's body, but can also be used for many other applications where the interaction is of fundamental importance. In the first set of experiments, after offline force reconstruction, we validated our model by comparing it with FT sensor data and benchmarked it against existing viscoelastic models. We showed that it is possible to reconstruct the contact force with high precision using different types of indenters and with more precision than it is currently possible using the Hunt-Crossley model. In the second set of experiments, we used an EKF to estimate online the point-wise elasticity of the silicone samples and compared the results with those from a compression test where the elasticity was computed offline. A comparison of the elasticity data obtained by compression testing and those obtained by indentation revealed an error of no more than 3% with respect to the adopted reference and with the spherical tip. This error is sufficiently small to differentiate between healthy and diseased tissue, which usually differ by at least one order of magnitude. To illustrate this point, consider the example of healthy breast tissue, its elastic modulus is 20 times less than the modulus of diseased tissue [41], [42]. Indeed, two types of rigid lumps, rendering cancerous inclusion in a tissue, were successfully identified, with one causing a 14% variation in elasticity. In the third set of experiments, continuous viscoelastic estimation was performed and compared with point-wise estimations, confirming the method's accuracy in dynamic palpation scenarios. We have shown that through dynamic estimation, although not highly precise in determining the absolute elastic modulus values, we were able to detect its very small variations. It has to be noted that the problem of the incorrect absolute elasticity estimates can be solved by checking the points of interest with the point estimation approach.

Future work will concentrate on integrating the dynamic estimation technique into a search algorithm for the location of tumours. Furthermore, it is planned to extend the tests from silicones to both healthy and diseased biological tissues, thus enabling comprehensive validation of this framework in the targeted use case of tumour detection and characterization.

## APPENDIX A

### GROUND TRUTH ELASTIC MODULUS MEASUREMENTS

Ground truth values for the elastic modulus used for comparison in Table IV were obtained performing compression tests on the cylindrical samples **S1** and **S2** with an Instron 4502 dynamometer. Given that the silicone materials under investigation are incompressible ( $\nu = 0.5$ ) [34], [36], the elastic modulus  $E_f$  cannot be simply obtained as the slope of the measured stress-strain curves, as the samples undergo complex deformations characterised by a bulging of their lateral surface. To extrapolate the value of the elastic modulus from the measurements, we performed a finite element simulation using Comsol Multiphysics (Nonlinear Structural Materials

module). We used a one-parameter Neo-Hooke incompressible hyperelastic model and simulated the compression behaviour of a sample with the same aspect ratio (diameter-to-height ratio) as the tested specimens. In the simulations, we assumed that the transverse bases of the samples are fixed in the radial direction and can only move relative to one another in the axial direction, whereas the lateral surface is free. Using the results from the FEM simulations, we found that for samples with diameter-to-height ratio of 2.32 the following stress-strain relationship holds:

$$P \simeq 1.75 E_f \varepsilon \quad (28)$$

where  $P$  is the nominal stress on the sample (force per unit nominal area) and  $\varepsilon$  is the lumped axial strain (displacement over initial height). The ground truth value of the elastic modulus  $E_f$  was obtained by fitting the data to the trend in (28).

#### ACKNOWLEDGMENT

This research has been funded by the MUR “Departments of Excellence 2023-27” program (L.232/2016), by the PNRR project FAIR - Future AI Research (PE00000013), and by the European Union projects INVERSE (GA no. 101136067) and MAGICIAN (GA no. 101120731).

#### REFERENCES

- [1] M. A. Al-Mouhamed, M. Nazeeruddin, and N. Merah, “Design and instrumentation of force feedback in telerobotics,” *IEEE Transactions on Instrumentation and Measurement*, vol. 58, no. 6, pp. 1949–1957, 2009.
- [2] L. Beber, E. Lamon, D. Nardi, D. Fontanelli, M. Saveriano, and L. Palopoli, “A passive variable impedance control strategy with viscoelastic parameters estimation of soft tissues for safe ultrasonography,” in *2024 IEEE International Conference on Robotics and Automation (ICRA)*, 2024, pp. 1298–1304.
- [3] J. F. Greenleaf, M. Fatemi, and M. Insana, “Selected methods for imaging elastic properties of biological tissues,” 2003.
- [4] A. Lau, M. L. Oyen, R. W. Kent, D. Murakami, and T. Torigaki, “Indentation stiffness of aging human costal cartilage,” *Acta Biomaterialia*, vol. 4, no. 1, 2008.
- [5] H. P. Dobrev, “In vivo study of skin mechanical properties in patients with systemic sclerosis,” *Journal of the American Academy of Dermatology*, vol. 40, no. 3, 1999.
- [6] A. Manduca, P. V. Bayly, R. L. Ehman, A. Kolipaka, T. J. Royston, I. Sack, R. Sinkus, and B. E. Van Beers, “MR elastography: Principles, guidelines, and terminology,” 2021.
- [7] S. Paul, S. Kumar Yadav, and M. Suheshkumar Singh, “Surface-Wave-Induced Photoacoustic Elastography in the Feasibility Study of Tissue Biomechanical Properties,” *IEEE Transactions on Instrumentation and Measurement*, vol. 73, pp. 1–10, 2024.
- [8] J. M. Pereira, J. M. Mansour, and B. R. Davis, “Dynamic measurement of the viscoelastic properties of skin,” *Journal of Biomechanics*, vol. 24, no. 2, pp. 157–162, 1 1991.
- [9] N. Frulio and H. Trillaud, “Ultrasound elastography in liver,” 2013.
- [10] G. Y. Li and Y. Cao, “Mechanics of ultrasound elastography,” 2017.
- [11] A. Tang, G. Cloutier, N. M. Szeverenyi, and C. B. Sirlin, “Ultrasound elastography and MR elastography for assessing liver fibrosis: Part 1, principles and techniques,” *American Journal of Roentgenology*, vol. 205, no. 1, 2015.
- [12] K. Kumar, M. E. Andrews, V. Jayashankar, A. K. Mishra, and S. Suresh, “Measurement of viscoelastic properties of polyacrylamide-based tissue-mimicking phantoms for ultrasound elastography applications,” *IEEE Transactions on Instrumentation and Measurement*, vol. 59, no. 5, pp. 1224–1232, 5 2010.
- [13] A. Eder, T. Arnold, and C. Kargel, “Performance evaluation of displacement estimators for real-time ultrasonic strain and blood flow imaging with improved spatial resolution,” *IEEE Transactions on Instrumentation and Measurement*, vol. 56, no. 4, 2007.
- [14] A. M. Cretu, P. Payeur, and E. M. Petriu, “Neural network mapping and clustering of elastic behavior from tactile and range imaging for virtualized reality applications,” *IEEE Transactions on Instrumentation and Measurement*, vol. 57, no. 9, pp. 1918–1928, 2008.
- [15] W. Flügge, *Viscoelasticity*. Berlin, Heidelberg: Springer Berlin Heidelberg, 1975.
- [16] A. Pappalardo, A. Albakri, C. Liu, L. Bascetta, E. De Momi, and P. Pognet, “Hunt-Crossley model based force control for minimally invasive robotic surgery,” *Biomedical Signal Processing and Control*, vol. 29, 2016.
- [17] X. Zhu, B. Gao, Y. Zhong, C. Gu, and K. S. Choi, “Extended Kalman filter for online soft tissue characterization based on Hunt-Crossley contact model,” *Journal of the Mechanical Behavior of Biomedical Materials*, vol. 123, 2021.
- [18] A. Haddadi and K. Hashtrudi-Zaad, “Real-time identification of hunt-crossley dynamic models of contact environments,” *IEEE Transactions on Robotics*, vol. 28, no. 3, pp. 555–566, 2012.
- [19] N. Diolaiti, C. Melchiorri, and S. Stramigioli, “Contact impedance estimation for robotic systems,” *IEEE Transactions on Robotics*, vol. 21, no. 5, pp. 925–935, 10 2005.
- [20] R. Schindeler and K. Hashtrudi-Zaad, “Online Identification of Environment Hunt-Crossley Models Using Polynomial Linearization,” *IEEE Transactions on Robotics*, vol. 34, no. 2, 2018.
- [21] L. Roveda, A. A. Shahid, N. Iannacci, and D. Piga, “Sensorless Optimal Interaction Control Exploiting Environment Stiffness Estimation,” *IEEE Transactions on Control Systems Technology*, vol. 30, no. 1, 2022.
- [22] X. Zhu, J. Li, Y. Zhong, K. S. Choi, B. Shirinzadeh, J. Smith, and C. Gu, “Iterative Kalman filter for biological tissue identification,” *International Journal of Robust and Nonlinear Control*, 2023.
- [23] W. C. Hayes, L. M. Keer, G. Herrmann, and L. F. Mockros, “A mathematical analysis for indentation tests of articular cartilage,” *Journal of Biomechanics*, vol. 5, no. 5, 1972.
- [24] M. Sakamoto, G. Li, T. Hara, and E. Y. Chao, “A new method for theoretical analysis of static indentation test,” *Journal of Biomechanics*, vol. 29, no. 5, 1996.
- [25] N. E. Waters, “The indentation of thin rubber sheets by cylindrical indentors,” *British Journal of Applied Physics*, vol. 16, no. 9, 1965.
- [26] E. K. Dimitriadis, F. Horkay, J. Maresca, B. Kachar, and R. S. Chadwick, “Determination of elastic moduli of thin layers of soft material using the atomic force microscope,” *Biophysical Journal*, vol. 82, no. 5, 2002.
- [27] V. L. Popov and M. Heß, *Method of dimensionality reduction in contact mechanics and friction*. Springer, 2015.
- [28] K. L. Johnson, *Contact mechanics*. Cambridge University Press, 1985.
- [29] L. Beber, E. Lamon, L. Palopoli, L. Fambri, M. Saveriano, and D. Fontanelli, “Elasticity measurements of expanded foams using a collaborative robotic arm,” in *2024 IEEE International Instrumentation and Measurement Technology Conference (I2MTC)*, 2024, pp. 1–6.
- [30] L. Beber, E. Lamon, G. Moretti, D. Fontanelli, M. Saveriano, and L. Palopoli, “Towards robotised palpation for cancer detection through online tissue viscoelastic characterisation with a collaborative robotic arm,” in *2024 IEEE/RSJ International Conference on Intelligent Robots and Systems (IROS)*, 2024.
- [31] Y. Bar-Shalom, X. R. Li, and T. Kirubarajan, *Estimation with applications to tracking and navigation: theory algorithms and software*. John Wiley & Sons, 2004.
- [32] J. J. Uicker, J. Denavit, and R. S. Hartenberg, “An iterative method for the displacement analysis of spatial mechanisms,” *Journal of Applied Mechanics, Transactions ASME*, vol. 31, no. 2, 1964.
- [33] “Guide to the expression of uncertainty in measurement,” 1995, ISO/IEC Guide 98-3:2008/Suppl 1:2008/Cor 1:2009 Uncertainty of measurement — Part 3: Guide to the expression of uncertainty in measurement (GUM:1995) — Supplement 1: Propagation of distributions using a Monte Carlo method, 2009.
- [34] P. N. Wells and H. D. Liang, “Medical ultrasound: imaging of soft tissue strain and elasticity,” *Journal of The Royal Society Interface*, vol. 8, no. 64, pp. 1521–1549, 11 2011.
- [35] Y. Yan and J. Pan, “Fast localization and segmentation of tissue abnormalities by autonomous robotic palpation,” *IEEE Robotics and Automation Letters*, vol. 6, pp. 1707–1714, 4 2021.
- [36] D. R. Darby, Z. Cai, C. R. Mason, and J. T. Pham, “Modulus and adhesion of sylgard 184, solaris, and ecoflex 00-30 silicone elastomers with varied mixing ratios,” *Journal of Applied Polymer Science*, vol. 139, no. 25, p. e52412, 2022.
- [37] B. Qiang, J. Greenleaf, M. Oyen, and X. Zhang, “Estimating material elasticity by spherical indentation load-relaxation tests on viscoelastic samples of finite thickness,” *IEEE Transactions on Ultrasonics, Ferroelectrics, and Frequency Control*, vol. 58, no. 7, 2011.

- [38] K. H. Kim, J. G. Lee, C. G. Park, and G. I. Jee, "The Stability Analysis of the Adaptive Fading Extended Kalman Filter," in *2007 IEEE International Conference on Control Applications*, 2007, pp. 982–987.
- [39] G. Hu, S. Gao, Y. Zhong, B. Gao, and A. Subic, "Modified strong tracking unscented Kalman filter for nonlinear state estimation with process model uncertainty," *International Journal of Adaptive Control and Signal Processing*, vol. 29, no. 12, pp. 1561–1577, 2015.
- [40] W. Othman, K. E. Vandyck, C. Abril, J. S. Barajas-Gamboa, J. P. Pantoja, M. Kroh, and M. A. Qasaimeh, "Stiffness assessment and lump detection in minimally invasive surgery using in-house developed smart laparoscopic forceps," *IEEE Journal of Translational Engineering in Health and Medicine*, vol. 10, pp. 1–10, 2022.
- [41] M. J. Paszek, N. Zahir, K. R. Johnson, J. N. Lakins, G. I. Rozenberg, A. Gefen, C. A. Reinhart-King, S. S. Margulies, M. Dembo, D. Boettiger *et al.*, "Tensional homeostasis and the malignant phenotype," *Cancer cell*, vol. 8, no. 3, pp. 241–254, 2005.
- [42] R. Xu, P. Yin, J. Wei, and Q. Ding, "The role of matrix stiffness in breast cancer progression: a review," *Frontiers in Oncology*, vol. 13, p. 1284926, 2023.



**Luca Beber** received his M.Sc. in Mechatronics Engineering in 2023. He is currently pursuing a Ph.D. within the DRIM doctoral programme in the Assistive and Medical Robotics of the University of Trento, focusing on control and motion planning of medical robotic arms for ultrasound and palpation examinations. His research interests include robotic manipulation, force-based interaction, and the development of robotic systems for medical applications.



**Edoardo Lamon** (Member, IEEE) received the Ph.D. degree in robotics from the University of Pisa, Pisa, Italy, in 2021. He is currently an Assistant Professor with the Department of Information Engineering and Computer Science, University of Trento, Trento, Italy, where he is the leading researcher of the Assistive and Medical Robotics group of the IDRA Labs. Until 2023, he acted as a postdoc with the Human–Robot Interfaces and Interaction (HRI<sup>2</sup>) group, IIT, Genoa, Italy. His interests lie in the intersection of human-robot collaboration, artificial

intelligence, robot control, and learning, with the aim of boosting robotics in human-populated environments in medical and industrial settings. Dr. Lamon was awarded as a finalist for the European best thesis in robotics at the Georges Giralt Ph.D. Award 2022 and as a finalist for the best paper award on mobile manipulation at IROS 2022. He serves as Associate Editor for the IEEE Robotics and Automation Letters and for International Conference on Ubiquitous Robots.



**Giacomo Moretti** holds an MSc degree in Energy Engineering, University of Pisa (2013) and a PhD in Mechanical Engineering, Scuola Sant'Anna, Pisa, Italy (2017). He has been a visiting scholar at the University of Edinburgh, UK (2016), and a research fellow at Scuola Sant'Anna (2017–2020) and at Saarland University, Germany (2020–2022) with a Marie-Curie fellowship. Currently, he is an Assistant Professor (with tenure track) in mechanics of machines at the University of Trento, Italy, where he leads a research group on multifunctional material

machines. His research interests cover the fields of multifunctional materials (especially electroactive polymers), energy harvesting, and soft robotics.



**Matteo Saveriano** (Senior Member, IEEE) is an Associate Professor of Control Engineering at the Department of Industrial Engineering of the University of Trento, Italy and the leading researcher of the Intelligent Robotics group of the IDRA Labs. He received the M.Sc. from the University of Naples "Federico II" in 2011 respectively, and a Ph.D. from the Technical University of Munich in 2017. After his Ph.D., he was a post-doctoral researcher at the German Aerospace Center (DLR) and a tenure-track assistant professor at the Department of Computer Science and at the Digital Science Centre of the University of Innsbruck. His research is at the intersection between learning and control and attempts to integrate cognitive robots into smart factories and social environments through the embodiment of AI solutions, inspired by human behaviour, into robotic devices. He serves regularly as Associate Editor for the main robotics conferences (ICRA, IROS, and HUMANOIDS) and for the IEEE Robotics and Automation Letters, the IEEE Transactions on Robotics, and for The International Journal of Robotics Research. He is the coordinator of the HE EU project INVERSE (GA 101136067).



**Luca Fambri** received the chemistry degree from the University of Parma, Parma, Italy, in 1985. He is currently an Associate Professor with the Department of Industrial Engineering, University of Trento, Trento, Italy, where he conducts research in polymer science and materials engineering. His research interests include polymer processing, additive manufacturing, fibre-reinforced composites, thermal energy storage materials, and biodegradable and recycled polymers, with applications spanning energy, sustainability, and biomedical fields. Prof. He is a member of the National Interuniversity Consortium for Materials Science and Technology (INSTM), the Italian Association for Materials Engineering (AIMAT), and the Italian Association of Macromolecules (AIM).



**Luigi Palopoli** (Senior Member, IEEE) received the Ph.D. degree in computer engineering from the Scuola Superiore Sant'Anna, Pisa, Italy, in 2002. He is a Full Professor and Director of the Department of Information Engineering and Computer Science, University of Trento, Trento, Italy. He has led several industrial and academic research projects, including H2020 ACANTO and FP7 DALi. He is the co-founder of Polytec Intralogistics Srl and of the IDRA Labs). His main research interests include robotics (with a particular focus on assistive robotics) and embedded system design (with a particular focus on language solutions and probabilistic techniques for soft real-time systems). Prof. Palopoli is currently Associate Editor for IEEE Transactions on Automatic Control and Elsevier Journal of System Architecture. He has also served on the programme committee of different conferences in the area of real-time and control systems.



**Daniele Fontanelli** (Fellow Member, IEEE) received the M.S. degree in Information Engineering in 2001, and the Ph.D. degree in Automation, Robotics and Bioengineering in 2006, both from the University of Pisa, Pisa, Italy. From 2008 he joined the University of Trento, Trento, Italy, where he is now a Full Professor in the field of measurement and robotics. He is currently a Senior Area Editor for the IEEE Transactions on Instrumentation and Measurement, an Associate Editor for the IEEE Robotics and Automation Letters, and he is a member of the IMEKO TC17 - Measurement in Robotics. He has also served in the technical program committee of numerous conferences in the area of measurements and robotics, and as an Associate Editor for the IET Science, Measurement & Technology Journal from 2019 to 2024. He is the co-founder of Polytec Intralogistics Srl and of the IDRA Labs). He is the PI of the EU project MAGICIAN and he was the co-founder and the PI of the EIT-Digital international Master on Autonomous Systems from 2017 to 2023. His research interests include distributed and real-time estimation and control, localisation algorithms, synchrophasor estimation, clock synchronisation algorithms, resource-aware control, wheeled mobile robots, service robotics and human-robot interaction and estimation.